EUROPEAN ORGANIZATION FOR NUCLEAR RESEARCH

CERN-PPE / 90-130
17 September 1990

MEASUREMENT OF THE TRANSVERSE ENERGY FLOW IN NUCLEUS–NUCLEUS COLLISIONS AT 200 GeV PER NUCLEON

HELIOS Collaboration

T. Åkesson[3], S. Almehed[6], A.L.S. Angelis[20], N. Armenise[1], H. Atherton[3], P. Aubry[8], H.W. Bartels[4], G. Beaudoin[8], J.M. Beaulieu[8], H. Beker[3], O. Benary[18], D. Bettoni[3,a], V. Bisi[19], I. Blevis[21], H. Bøggild[3,b], W. Cleland[12], M. Clemen[12], B. Collick[12], F. Corriveau[7], S. Dagan[18], K. Dederichs[3,c], S. Dell'Uomo[13], P. Depommier[8], R.C.E. Devenish[3,d], N. DiGiacomo[5], S. DiLiberto[13], J.R. Dodd[20], B. Dolgoshein[10], A. Drees[4], H. En'yo[3], B. Erlandsson[17], M.J. Esten[20], C.W. Fabjan[3], P. Fischer[4], Z. Fraenkel[21], A. Gaidot[15], F. Gibrat-Debu[15], P. Giubellino[19], P. Glassel[4], U. Goerlach[3], R. Haglund[6], L.A. Hamel[7], H. van Hecke[5], V. Hedberg[3], R. Heifetz[18], A. Holscher[4], B. Jacak[5], G. Jarlskog[6], S. Johansson[6], H. Kraner[2], V. Kroh[4], F. Lamarche[7], C. Leroy[7], D. Lissauer[2,18], G. London[15], B. Lorstad[6], A. Lounis[8], F. Martelli[19,h], A. Marzari-Chiesa[19], M. Masera[19], M.A. Mazzoni[3], E. Mazzucato[7], N.A. McCubbin[14], P. McGaughey[5], F. Meddi[13], U. Mjörnmark[6], M.T. Muciaccia[1], S. Muraviev[9], M. Murray[12], M. Neubert[4], S. Nilsson[17], L. Olsen[2], Y. Oren[18], J.P. Pansart[15], Y.M. Park[12], A. Pfeiffer[4], F. Piuz[3], V. Polychronakos[2], G. Poulard[3], M. Price[3], D. Rahm[2], L. Ramello[19], L. Riccati[19], G. Romano[16], G. Rosa[13], L. Sandor[3], J. Schukraft[3], M. Sekimoto[3,e], B. Sellden[17], M. Seman[3,f], A. Shmeleva[9], V. Sidorov[11], S. Simone[1], Y. Sirois[7], H. Sletten[3], S. Smirnov[10], W. Sondheim[5], H.J. Specht[4], I. Stumer[2], J.W. Sunier[5], V. Tcherniatin[10], H.H. Thodberg[3], J. Thompson[12], V. Tikhomirov[9], I. Tserruya[21], G. Vasseur[15], R.J. Veenhof[3,g], R. Wigmans[3,g], P. Yepes[7] and W.J. Willis[3]

Abstract

The transverse energy distributions have been measured for interactions of ^{32}S nuclei with Al, Ag, W, Pt, Pb, and U targets, at an incident energy of 200 GeV per nucleon in the pseudorapidity region $-0.1 < \eta_{lab} < 5.5$. These distributions are compared with those for ^{16}O–W interactions in the same pseudorapidity region and with earlier measurements performed with ^{16}O and ^{32}S projectiles in the region $-0.1 < \eta_{lab} < 2.9$. These comparisons provide both a better understanding of the dynamics involved and improved estimates of stopping power and energy density.

(Submitted to Nuclear Physics B)

1) University of Bari and INFN, I-70100 Bari, Italy
2) Brookhaven National Laboratory, Upton, NY 11973, USA
3) CERN, CH-1211 Geneva 23, Switzerland
4) University of Heidelberg, D-6900 Heidelberg, Fed. Rep. Germany
5) Los Alamos National Laboratory, Los Alamos NM87544, USA
6) University of Lund, S-223 62 Lund, Sweden
7) McGill University, Montreal, PQ H3A 2T8 Canada
8) University of Montreal, Montreal PQ HC3 3J7 Canada
9) Lebedev Institute of Physics, SU-117924 Moscow, USSR
10) Institute of Physics and Engineering, SU-115409 Moscow, USSR
11) Institute of Nuclear Physics, 630 090 Novosibirsk, USSR
12) University of Pittsburgh, Pittsburgh PA 15260, USA
13) University of Rome 'La Sapienza' and INFN, I-00185 Rome, Italy
14) Rutherford Appleton Laboratory, Didcot OX1 OQX, UK
15) DPhPE, CEN–Saclay, F-91191 Gif-sur-Yvette, France
16) University of Salerno and INFN, I-84100 Salerno, Italy
17) University of Stockholm, S-11346, Stockholm, Sweden
18) University of Tel Aviv, Ramat Aviv 9978 Israel
19) University of Turin and INFN, I-10100 Turin, Italy
20) University College London, London WC1E 6BT, UK
21) Weizmann Institute, 76 100 Rehovot, Israel
a) Visitor at CERN from: University of Syracuse, Syracuse, NY 13244-1130, USA
b) Visitor at CERN from: Niels Bohr Institute, DK-2100 Copenhagen 0, Denmark
c) Visitor at CERN from: Ludwig–Maximilians–Universität, D-8000 Munich 40, Fed. Rep. Germany
d) Visitor at CERN from: Oxford University, Oxford OX1 3NP, UK
e) Visitor at CERN from: Institute of Nuclear Study, Tokyo 188, Japan
f) Visitor at CERN from: Slovak Academy of Sciences, CS-04353 Kosice, Czechoslovakia
g) Visitor at CERN from: NIKHEF-H, NL-1009 DB Amsterdam, The Netherlands.
h) 'Angelo Della Riccia' Fellow

1. INTRODUCTION

The measurement of transverse energy produced in nucleus–nucleus collisions at high energies allows the selection of collisions yielding very dense hadronic matter. If the energy density is high enough, the hadronic matter may undergo a phase transition into a state of deconfined quarks and gluons [1]. The energy densities reached depend, among other factors, on the degree of stopping which occurs in each collision.

This article presents the results of our measurements on the transverse energy (E_T) with a nearly complete coverage of pseudorapidity. The maximum energy densities achieved in ^{16}O and ^{32}S–W collisions have been previously estimated [2, 3] from the measurement of the maximum transverse energy in the backward region and from using estimates of the relative contribution of E_T in the forward region. The new measurements provide a check on the validity of these estimates. In addition, the study of the event-by-event correlation between the forward and backward transverse energies as a function of the full E_T sheds light on the reaction dynamics. The dependence of the $d\sigma/dE_T$ and the $dE_T/d\eta$ distributions on the target and projectile is studied. Estimates of the maximum stopping and energy density reached in ^{16}O–W and ^{32}S–W collisions are also obtained from the maximum value of the total transverse energy measured in the full region.

2. THE EXPERIMENTAL SET-UP

The HELIOS (High-Energy Lepton and IOn Spectrometer) detector measures the transverse energy in the backward region using uranium/scintillator and iron/scintillator sampling calorimeters, and in the forward region using a uranium/liquid-argon calorimeter (ULAC). The backward transverse energy ($\equiv E_T^{back}$) is defined for $-0.1 < \eta_{lab} < 2.9$, whereas the forward transverse energy ($\equiv E_T^{forw}$) is defined for $2.9 < \eta_{lab} < 5.5$ the 'Full' region ≡ 'Backward' + 'Forward'.

The uranium/scintillator calorimeters have a 20 × 20 cm² tower structure, for both the electromagnetic and hadronic sections. The calibration and the method of analysis of the scintillator calorimeters have been described elsewhere [2–4].

The electromagnetic (e.m.) part of ULAC starts 3.8 m downstream from the target and has a 5 cm diameter hole to permit the projectile fragments to pass without interactions. This section has 1920 towers, most of them 2 × 2 cm² except for larger guard areas around the periphery of its acceptance, and it has two sections in depth, 7 and 14 radiation lengths, respectively. The hadronic (had) section, just behind the e.m. section, has no hole, it has 2.5 cm wide strips in the horizontal and vertical directions transverse to the beam, and it is divided in depth into three sections, each about 1.5 interaction lengths deep. The ULAC was calibrated with electron and pion beams of momenta of 17, 45, 70, and 200 GeV/c. The calibration showed an average e/π ratio of about 1.10 ± 0.03 and a hadronic energy resolution of $\sigma/E(\text{GeV}) = 0.015 + 0.45/\sqrt{E}$ for fully contained showers.

Downstream from the target, a set of three silicon ring counters (R_1, R_2, and R_3) [3, 5] are used, as indicated below, to separate target interactions from background generated in the beam-pipe window, in the air, and in the detectors themselves.

3. THE DATA SETS

During the 1987 HELIOS runs, the following numbers of triggers were collected: 15,000 O–W, 19,000 S–Al, 22,000 S–Ag, 26,400 S–W, 24,000 S–Pt, 15,000 S–Pb, and 23,000 S–U. The samples of sulphur events were filtered to remove a) events with two simultaneous beam particles, characterized by an anomalous measured total energy, b) upstream interactions, characterized by highly correlated hits in the ring counter detectors [3], and c) downstream interactions characterized by $M_{R3} > 1.1M_{R1} + 10$ and $M_{R1} < 40$, where M_{R3} and M_{R1} are the multiplicities of the most downstream and the most upstream ring detector, respectively. The oxygen sample was filtered using cuts similar to those used in ref. [2]. The remaining contamination is removed by the subtraction of spectra obtained without any

target [3]. This contamination is negligible for the highest values of E_T, but amounts to typically 20% for $E_T < 25$ GeV.

4. DATA ANALYSIS

The forward transverse energy E_T^{forw} is calculated by a weighted sum of the energies found in individual towers of the e.m. section and in individual strips of the hadronic section of ULAC: $E_T^{forw} = E_T^{forw}(e.m.) + E_T^{forw}(had)$ [6]. The e.m. contribution to E_T^{forw} is straightforward:

$$E_T^{forw}(e.m.) = \Sigma\, s_i E_i \ ,$$

where s_i is the sine of the polar angle of the i^{th} tower, measuring energy E_i.

The hadronic contribution to E_T^{forw} is complicated by the lateral spread of the showers due to the projectile fragments. To understand this effect, we have studied the shower profiles produced by sulphur ions and protons interacting at the centre of the hadronic section of ULAC. The average shower profiles for protons and sulphur ions are quite similar (fig. 1). The two central strips are excluded from the determination of E_T^{forw}, limiting the pseudorapidity acceptance to $\eta \leq 5.5$, but the measured energies in these strips are used, event-by-event, to correct for leakage into neighbouring strips of the energy deposited by nuclear fragments. To correct approximately for this leakage, the hadronic contribution to E_T^{forw} is experimentally defined as

$$E_T^{forw}(had) = \pi/2[\, \Sigma\, X_i\, (E_{x_i} - \beta_i E_{x_0}) + \Sigma\, Y_j\, (E_{y_j} - \beta_j E_{y_0})\,],$$

where X_i (Y_j) is the sine of the polar angle of the geometric centre of the i^{th} x-strip (j^{th} y-strip), E_{x_i} (E_{y_j}) is the energy measured in that strip, and β_i (β_j) is the fraction of the energy of the central energy slab energy E_{x_0} (E_{y_0}) in the i^{th} (j^{th}) strip as determined in fig. 1. Assuming azimuthal symmetry, the factor $\pi/2$ corrects for the effect of the Cartesian readout of the hadronic section of ULAC.

The correspondence between the experimental definition of E_T^{forw} and the true one has been investigated in a Monte Carlo simulation. We used an event generator [2], to which was added the fragment simulation of ref. [7] in order to determine the sensitivity of E_T to projectile fragments, to the particle mix, and to the momentum distributions. The converted energy is defined as the kinetic energy of the baryons and the total energy of all other particles including the antibaryons. The calorimeter simulation included the response to different particles (e/π), the energy leakage (affecting the energy scale), and the resolution (affecting the shape). The evaluation of the systematic uncertainty included that already evaluated for the backward direction (7.1%) [2] as well as the errors in the evaluation of the forward E_T, which were due to the following: subtraction of leakage of fragment energy (2%), calibration (2%), particle composition (3%), and e/π ratio (3%). The combined systematic uncertainty on the E_T^{forw} scale is 5.0%. Our data on the almost symmetrical system ^{32}S–^{27}Al were used to check our evaluation of E_T^{forw} relative to E_T^{back} as a function of E_T, and was found to be consistent with the expectation.

To compute the pseudorapidity density of E_T, a pseudorapidity must be attributed to each channel of ULAC. There is a unique pseudorapidity for each tower of the e.m. section, but each strip of the hadronic section covers a rather large range in pseudorapidity. The Monte Carlo calculation shows that the pseudorapidity is correctly measured, on the average, if we give each strip the pseudorapidity of its centre minus 0.31. An effective pseudorapidity resolution of 0.2 in most of ULAC and of 0.4 near η = 5.5 is attained.

5. RESULTS

5.1 Target dependence

The differential cross-sections $d\sigma/dE_T$ in the full region are presented as a function of E_T in fig. 2 and in tables 1 to 6 for collisions of ^{32}S with various target nuclei at an incident energy of 200 GeV per nucleon. For all targets, the E_T distributions have the shape that was previously observed for incident oxygen and sulphur beams in the backward region [2, 3]: a plateau (shorter for the Al target) followed by a steeply falling tail.

The maximum values of E_T obtained in the full region (from $E_T \approx 190$ GeV for ^{32}S–Al to $E_T \approx 470$ GeV for ^{32}S–U) are substantially larger than the values found [2, 3] in the backward region (≈ 94 GeV and ≈ 339 GeV, respectively). The E_T measured with full coverage, relative to that in the backward region, increases consistently more for average central collisions (defined as the value of E_T for which $d\sigma/dE_T$ is 1/2 of the plateau value) than for the high-E_T tail. For example, in ^{32}S–W collisions at 200 GeV per nucleon, the extension from the backward to the full region increases E_T for average central collisions from 198 to 327 GeV, and from 310 to 445 GeV in the tail (fig. 3). The E_T distributions for 200 GeV per nucleon ^{32}S on W targets are compared in fig. 3 with the predictions of the FRITIOF 1.6 [8] and IRIS 3.05 [9] event generators. FRITIOF uses independent nucleon–nucleon interactions, whilst IRIS is based on colour exchange, with the dual parton model [9] as the starting point. Both models use the Lund fragmentation model [10]. The E_T in the forward rapidity region is somewhat overestimated in the tail of the distribution by the IRIS generator. In the full and backward regions, and for both projectiles, the models reproduce the plateau in a satisfactory fashion, but fall short, by about 15%, of describing the extent of the tail. This may be due to an underestimation of the stopping power and/or to cascading in the target nucleus, not included in the models.

The target mass dependence of $E_T^{central}$ can be fitted to the form A^α [2, 3]. The value of α varies with the pseudorapidity window and decreases from $\alpha \approx 0.5$ in the backward region [3] (0.48 ± 0.02 and 0.53 ± 0.04 for ^{16}O at 60 and 200 GeV per nucleon, respectively, and 0.53 ± 0.05 for ^{32}S at 200 GeV per nucleon), to $\alpha = 0.39 \pm 0.01$ (for ^{32}S at 200 GeV) in the full region. The latter value is closer to $\alpha = 1/3$ expected from naïve scaling with target nucleus thickness, and was also reported by the WA80 and NA35 [11] experiments. The rise of $E_T^{central}$ with A is generally interpreted as a sign of 'partial stopping', since, in the case of full stopping, $E_T^{central}$ would cease to rise beyond a certain size of the target.

Full stopping, however, is observed at lower energies, e.g. at BNL in collisions at $\sqrt{s_{NN}} = 5$ GeV, already in medium-size nuclear targets [12].

5.2 Forward versus backward transverse energy deposition

Figure 4 shows a contour plot of the event-by-event differential cross-sections for E_T^{forw} versus E_T^{back} for S–W collisions. The most probable E_T^{forw} is proportional to E_T^{back} up to a value close to $E_T^{central}$, where the sulphur nucleus fully overlaps the target. Beyond this, E_T^{forw} appears to be saturated and is independent of E_T^{back}. This saturation can be interpreted in several ways: for example, a) after full overlap, the number of participating projectile nucleons no longer increases, while that for the target continues to increase; the backward rapidity shift occurring when more target nucleons are participating forces E_T^{forw}/E_T to decrease, so that E_T^{forw} is approximately independent of E_T^{back} at large enough E_T or b) the production mechanism for E_T^{forw} is independent of the production mechanism for E_T^{back} [13]. The IRIS prediction for one of the contours is shown; the overshoot in E_T^{forw} is apparent and there is less saturation in the IRIS prediction. Perhaps this is a consequence of an underestimate of stopping and/or cascading.

One would expect the tails of $d\sigma/dE_T$ of the E_T^{forw} distribution to be considerably steeper than those of E_T^{back}, and fig. 3 shows that this is indeed the case. The saturation of E_T^{forw} means that the width of the tail of $d\sigma/E_T^{forw}$ is determined only by the event-to-event fluctuations in E_T^{forw} and is

independent of the S–W geometry. The widths of the contours of fig. 4 reflect the magnitude of the event-to-event fluctuations of E_T^{forw} versus E_T^{back}. Analysis of the contours shows that for central collisions the r.m.s. width of the event-to-event fluctuations in E_T^{forw} is 12–15 GeV, or about 10%. The contour widths do not depend strongly on the transverse energy; the fluctuations in E_T^{forw} for peripheral collisions (low values of E_T^{back}) are about 10 GeV.

5.3 Projectile dependence

Comparison with the data taken with incident ^{16}O illustrate the dependence of E_T production on projectile mass. The E_T differential cross-section for ^{16}O–W collisions is given in table 7 and compared with that for ^{32}S–W collisions in fig. 5. The increase of E_T for ^{32}S over ^{16}O is 62% for average central collisions and 55% in the tail.

An estimate of the maximum stopping fraction S can be obtained from the ratio $S(E_T) \equiv E_T / E_T^{avail}$. We determine E^{avail} by distributing the available energy according to our measured $dE_T/d\eta$ for the highest E_T [14] [where $E^{avail} = \sqrt{s} - m(N_p + N_t)$ is the available centre-of-mass energy, with $s \sim 2 \times 200 \times N_p \times N_t \times m$ GeV^2; N_p and N_t are the number of participating projectile and target nucleons, respectively, and m is the nucleon mass]. The values of S for E_T such that $d\sigma/dE_T$ reaches 10^{-4} times the plateau value in the full region are reported in table 8 for various projectiles and targets. It is seen that S increases with the target thickness but does not vary much with the size of the projectile. A similar calculation shows that even at an incident energy of 60 GeV per nucleon the full stopping limit ($S = 1$) is not reached.

The energy density can be estimated, assuming that the initially available energy is deposited in the relevant interaction volume V, often taken to be the geometric Lorentz-contracted volume. The energy density $\varepsilon = \gamma (E_T^{meas} V)$ (where $\gamma \sim E_{beam}/\sqrt{s}$) is $\sim$ 5.5 GeV/fm^3 and $\sim$ 6.8 GeV/fm^3 in the tails of the ^{16}O–W and ^{32}S–W distributions, respectively, consistent with earlier estimates [2, 3]. See subsection 5.4 for another estimate.

5.4 Pseudorapidity distributions

The pseudorapidity distributions for ^{16}O–W and ^{32}S–W collisions are shown in fig. 6. Whilst the shape of the distribution for each projectile in the backward region does not change very much with increasing E_T, most of the increase of E_T is in this region. The relative contribution of the forward region changes with the projectile mass and with E_T. For both projectiles, fig. 7 shows that the average pseudorapidity shifts forward with increasing projectile mass and shifts backward with increasing E_T. The maximum $dE_T/d\eta$ value rises somewhat more rapidly than E_T.

The comparisons to IRIS, shown in fig. 6, are made with samples for E_T values corresponding to the same $d\sigma/dE_T$ as the data. The trend is the same for both projectiles: there is a large underestimate in the backward region for all E_T^{full} whilst, in the forward region, the predictions are good for the plateau region but there is an increasing small overestimate as E_T^{full} increases.

An estimate of the error in the energy density determined above can be obtained by calculating the energy density in the Bjorken longitudinal hydrodynamic limit [15]: $\varepsilon = 1/A\tau \, (dE_T/d\eta)_{max}$, where A is the cross-sectional area of the (smaller) projectile and τ is the expansion time, whose value is traditionally assumed to be $\sim$ 1 fm/c. The corresponding values in this limit are $\sim$ 3.0 GeV/fm^3 and $\sim$ 3.4 GeV/fm^3.

In fig. 7 we also give the r.m.s. widths of the measured $dE_T/d\eta$ distributions. As E_T increases, the width of the pseudorapidity distribution does not approach that expected for an isotropic distribution[1] but is always larger. The corresponding value in pp collisions is measured to be $\sigma = 1.7$ [16]. Such a

[1] In the case of isotropy, $dE_T/d\eta$ approaches the form $1/\cosh^3(\eta-\eta_0)$, which has an r.m.s. width = 0.7.

considerably larger width would be expected if the system of high energy density were to undergo a longitudinal expansion prior to emission of the particles. In the simplest case, one may consider a one-dimensional longitudinal expansion, as discussed by Landau [17] and more recently in ref. [18]. In this picture, the width depends on the ratio of the initial and final temperatures. Within this framework the expansion time is evaluated to be approximately $\tau \approx 8$ fm/c [17], compatible with an independent determination based on Bose–Einstein interferometry [19]. However, a microscopic model such as FRITIOF also predicts r.m.s. widths of the order of 1.2, as can be seen from fig. 7. Thus we cannot make a clear distinction between the macroscopic and microscopic approaches.

6. CONCLUSION

In conclusion, we have presented our measurements of E_T with a nearly complete coverage of pseudorapidity. It was observed that for large target nuclei, E_T^{max} in the full region is largely determined by E_T in the backward region since, as the total E_T increases, E_T in the forward region becomes independent of that in the backward one. Thus E_T measured with a backward coverage or with a full coverage are equivalently good triggers for selecting high-energy density. The pseudorapidity distributions do not approach those for an isotropic fireball even at the highest measured E_T, but are always considerably broader. The evaluated stopping fractions increase with the atomic number of the target, reaching values as high as 0.9. However, stopping does not appear to depend greatly on the size of the projectile; this could be because oxygen and sulphur nuclei are small relative to the heavy targets that we have investigated in detail. The estimated energy density is within the range of values predicted for the onset of the deconfinement phase transition [1].

Acknowledgements

The HELIOS Collaboration acknowledges the dedication and excellent work of the staff of the CERN PS–SPS accelerator complex in providing ion beams of very high quality.

We thank the technical staff of CERN, and of the institutes collaborating in HELIOS, for their invaluable contributions.

We are grateful for the support given by the Natural Sciences and Engineering Research Council of Canada, the Institut de Recherche Fondamentale (CEA, France), the German Federal Minister for Research and Technology, the Istituto Nazionale di Fisica Nucleare of Italy, the Science Research Council of Sweden, the Science and Engineering Research Council of the United Kingdom, the US Department of Energy, and the US–Israel Binational Science Foundation.

REFERENCES

[1] See the following 'Quark Matter' Proceedings:
T.W. Ludlam and H.E. Wegner (eds.), Brookhaven, 1983 [Nucl. Phys. **A418** (1984)].
K. Kajantje (ed.), Helsinki, 1984 [Lecture Notes in Physics **221** (1984): Springer Verlag, Heidelberg].
M. Gyulassy (ed.), Asilomar, 1986 [Nucl. Phys. **A461** (1987)].
H. Satz, H.J. Specht and R. Stock (eds.), Nordkirchen, 1987 [Z. Phys. **C38** (1988)].
G. Baym, P. Braun-Munzinger and S. Nagamiya (eds.), Lennox, 1988 [Nucl. Phys. **A498** (1989)].

[2] T. Åkesson et al. (HELIOS Collab.), Z. Phys. **C38** (1988) 383.

[3] T. Åkesson et al. (HELIOS Collab.), Phys. Lett. **B214** (1988) 295.

[4] T. Åkesson et al., Nucl. Instrum. Methods **A262** (1987) 243.

[5] P. Giubellino et al., Nucl. Instrum. Methods **A275** (1989) 89.

[6] For more details concerning the analysis, see F. Lamarche, Ph.D. thesis, McGill University, Montreal (1989).

[7] B. Nilsson-Almqvist and E. Stenlund, Comput. Phys. Commun. **43** (1987) 387.
B. Andersson et al., Nucl. Phys. **B281** (1987) 289.
B. Andersson, G. Gustafson and T. Sjöstrand, Z. Phys. **C6** (1980) 235.

[8] J.P. Pansart, CEN–Saclay report DPhPE 89–04 (1989).

[9] A. Capella and J. Tran Thanh Van, Phys. Lett. **B93** (1980) 146.

[10] B. Andersson, G. Gustafson and T. Sjöstrand, Z. Phys. **C6** (1980) 235.

[11] R. Albrecht et al., Phys. Lett. **B202** (1988) 596.

[12] A. Bamberger et al., Phys. Lett. **B205** (1988) 583.

[13] A. Dar and J. Vary, Phys. Rev. **D6** (1972) 2412.

[14] J. Stachel and P. Braun-Munzinger, Phys. Lett. **B216** (1989) 1.

[15] J.D. Bjorken, Phys. Rev. **D27** (1983) 140.

[16] C. de Marzo et al., Phys. Rev. **D26** (1982) 1019.

[17] L.D. Landau, paper No. 74 in Collected papers of L.D. Landau, ed. D. Ter Haar (Pergamon Press, Oxford, 1965), p. 569. [Izv. Akad. Nauk, Ser. Fiz. **17** (1953) 51.]

[18] F. Lamarche and C. Leroy, Longitudinal expansion of hadronic matter in high-energy nuclear collisions, contribution to the Hadronic Session of the 24th Rencontre de Moriond, Les Arcs, 1989, ed. J. Tran Thanh Van.

[19] T.J. Humanic et al. (NA35 Collab.), Z. Phys. **C38** (1988) 79.
J.W. Harris et al. (NA35 Collab.), Nucl. Phys. **A498** (1989) 133c.

Table 1

The transverse-energy differential cross-section $d\sigma/dE_T$ in the full region for 200 GeV per nucleon ^{32}S–Al collisions

E_T [GeV]	Bin half-width [GeV]	$d\sigma/dE_T$ [mb/GeV]	Error [mb/GeV]
36.5	2.4	$9.94 \times 10^{+0}$	4.68×10^{-1}
41.4	2.4	$9.07 \times 10^{+0}$	4.52×10^{-1}
46.2	2.4	$9.13 \times 10^{+0}$	4.44×10^{-1}
51.1	2.4	$9.27 \times 10^{+0}$	4.35×10^{-1}
56.0	2.4	$8.62 \times 10^{+0}$	4.16×10^{-1}
60.8	2.4	$8.75 \times 10^{+0}$	4.12×10^{-1}
65.7	2.4	$7.07 \times 10^{+0}$	3.77×10^{-1}
70.6	2.4	$6.87 \times 10^{+0}$	3.71×10^{-1}
75.4	2.4	$6.75 \times 10^{+0}$	3.57×10^{-1}
80.3	2.4	$5.41 \times 10^{+0}$	3.26×10^{-1}
85.2	2.4	$5.65 \times 10^{+0}$	3.20×10^{-1}
90.0	2.4	$5.69 \times 10^{+0}$	3.16×10^{-1}
94.9	2.4	$4.96 \times 10^{+0}$	2.87×10^{-1}
99.8	2.4	$4.81 \times 10^{+0}$	2.79×10^{-1}
104.6	2.4	$4.74 \times 10^{+0}$	2.70×10^{-1}
109.5	2.4	$4.50 \times 10^{+0}$	2.61×10^{-1}
114.4	2.4	$3.97 \times 10^{+0}$	2.45×10^{-1}
119.2	2.4	$3.74 \times 10^{+0}$	2.38×10^{-1}
124.1	2.4	$2.98 \times 10^{+0}$	2.11×10^{-1}
129.0	2.4	$2.94 \times 10^{+0}$	2.07×10^{-1}
133.8	2.4	$2.41 \times 10^{+0}$	1.87×10^{-1}
138.7	2.4	$1.76 \times 10^{+0}$	1.72×10^{-1}
143.6	2.4	$1.92 \times 10^{+0}$	1.72×10^{-1}
148.4	2.4	$1.44 \times 10^{+0}$	1.49×10^{-1}
153.3	2.4	$1.02 \times 10^{+0}$	1.24×10^{-1}
158.2	2.4	5.31×10^{-1}	8.87×10^{-2}
163.0	2.4	4.90×10^{-1}	8.66×10^{-2}
167.9	2.4	3.99×10^{-1}	8.99×10^{-2}
172.8	2.4	2.40×10^{-1}	7.43×10^{-2}
177.6	2.4	1.15×10^{-1}	4.19×10^{-2}
182.5	2.4	6.07×10^{-2}	7.83×10^{-3}
187.4	2.4	2.92×10^{-2}	6.21×10^{-3}
192.2	2.4	1.23×10^{-2}	4.74×10^{-3}
197.1	2.4	4.08×10^{-3}	3.71×10^{-3}

Table 2

The transverse-energy differential cross-section $d\sigma/dE_T$ in the full region for 200 GeV per nucleon ^{32}S–Ag collisions

E_T [GeV]	Bin half-width [GeV]	$d\sigma/dE_T$ [mb/GeV]	Error [mb/GeV]
4.7	4.7	$3.30 \times 10^{+2}$	$2.58 \times 10^{+2}$
14.1	4.7	$8.22 \times 10^{+1}$	$6.59 \times 10^{+1}$
23.5	4.7	$2.36 \times 10^{+1}$	$3.07 \times 10^{+0}$
38.1	9.4	$1.54 \times 10^{+1}$	$1.95 \times 10^{+0}$
51.7	4.7	$8.91 \times 10^{+0}$	$2.69 \times 10^{+0}$
61.1	4.7	$9.53 \times 10^{+0}$	$2.50 \times 10^{+0}$
79.9	14.1	$4.83 \times 10^{+0}$	$1.17 \times 10^{+0}$
108.2	14.1	$2.76 \times 10^{+0}$	8.78×10^{-1}
127.0	4.7	$6.02 \times 10^{+0}$	$1.49 \times 10^{+0}$
145.8	14.1	$4.40 \times 10^{+0}$	7.80×10^{-1}
164.6	4.7	$3.64 \times 10^{+0}$	8.83×10^{-1}
174.0	4.7	$4.31 \times 10^{+0}$	9.89×10^{-1}
183.4	4.7	$4.65 \times 10^{+0}$	$1.10 \times 10^{+0}$
192.8	4.7	$4.15 \times 10^{+0}$	2.08×10^{-1}
202.2	4.7	$4.15 \times 10^{+0}$	2.08×10^{-1}
211.6	4.7	$4.14 \times 10^{+0}$	2.08×10^{-1}
221.0	4.7	$3.65 \times 10^{+0}$	1.96×10^{-1}
230.4	4.7	$3.51 \times 10^{+0}$	1.92×10^{-1}
239.8	4.7	$3.17 \times 10^{+0}$	1.83×10^{-1}
249.2	4.7	$2.97 \times 10^{+0}$	1.76×10^{-1}
258.6	4.7	$2.72 \times 10^{+0}$	1.72×10^{-1}
268.1	4.7	$2.66 \times 10^{+0}$	1.67×10^{-1}
277.5	4.7	$1.92 \times 10^{+0}$	1.42×10^{-1}
286.9	4.7	$1.65 \times 10^{+0}$	1.31×10^{-1}
296.3	4.7	9.89×10^{-1}	1.01×10^{-1}
305.7	4.7	5.40×10^{-1}	7.43×10^{-2}
315.1	4.7	3.48×10^{-1}	2.24×10^{-2}
324.5	4.7	1.78×10^{-1}	1.58×10^{-2}
333.9	4.7	7.33×10^{-2}	9.88×10^{-3}
343.3	4.7	2.33×10^{-2}	4.01×10^{-3}
352.7	4.7	8.69×10^{-3}	2.25×10^{-3}
362.1	4.7	1.33×10^{-3}	9.41×10^{-4}

Table 3

The transverse-energy differential cross-section $d\sigma/dE_T$ in the full region for 200 GeV per nucleon ^{32}S–W collisions

E_T [GeV]	Bin half-width [GeV]	$d\sigma/dE_T$ [mb/GeV]	Error [mb/GeV]
32.9	4.7	$1.25 \times 10^{+1}$	$1.75 \times 10^{+0}$
42.3	4.7	$1.58 \times 10^{+1}$	$1.45 \times 10^{+0}$
51.7	4.7	$1.13 \times 10^{+1}$	$1.45 \times 10^{+0}$
61.1	4.7	$1.00 \times 10^{+1}$	$1.32 \times 10^{+0}$
70.5	4.7	$1.06 \times 10^{+1}$	$1.24 \times 10^{+0}$
79.9	4.7	$8.97 \times 10^{+0}$	$1.00 \times 10^{+0}$
89.4	4.7	$5.63 \times 10^{+0}$	$9.91 \times 10^{+0}$
98.8	4.7	$7.10 \times 10^{+0}$	8.68×10^{-1}
108.2	4.7	$6.02 \times 10^{+0}$	7.87×10^{-1}
117.6	4.7	$7.11 \times 10^{+0}$	6.82×10^{-1}
127.0	4.7	$7.66 \times 10^{+0}$	4.75×10^{-1}
136.4	4.7	$6.78 \times 10^{+0}$	3.68×10^{-1}
145.8	4.7	$7.38 \times 10^{+0}$	3.25×10^{-1}
155.2	4.7	$7.00 \times 10^{+0}$	3.15×10^{-1}
164.6	4.7	$6.76 \times 10^{+0}$	3.15×10^{-1}
174.0	4.7	$6.19 \times 10^{+0}$	3.02×10^{-1}
183.4	4.7	$5.98 \times 10^{+0}$	2.96×10^{-1}
192.8	4.7	$6.18 \times 10^{+0}$	3.02×10^{-1}
202.2	4.7	$6.06 \times 10^{+0}$	3.00×10^{-1}
211.6	4.7	$5.14 \times 10^{+0}$	1.11×10^{-1}
221.0	4.7	$4.61 \times 10^{+0}$	7.95×10^{-1}
230.4	4.7	$4.67 \times 10^{+0}$	7.93×10^{-2}
239.8	4.7	$5.10 \times 10^{+0}$	7.11×10^{-2}

(Cont.)

Table 3 (Cont.)

E_T [GeV]	Bin half-width [GeV]	$d\sigma/dE_T$ [mb/GeV]	Error [mb/GeV]
249.2	4.7	$4.98 \times 10^{+0}$	7.02×10^{-2}
258.6	4.7	$4.93 \times 10^{+0}$	6.97×10^{-2}
268.1	4.7	$4.99 \times 10^{+0}$	7.02×10^{-2}
277.5	4.7	$4.96 \times 10^{+0}$	7.05×10^{-2}
286.9	4.7	$4.81 \times 10^{+0}$	6.90×10^{-2}
296.3	4.7	$4.66 \times 10^{+0}$	6.77×10^{-2}
305.7	4.7	$4.32 \times 10^{+0}$	6.49×10^{-2}
315.1	4.7	$4.06 \times 10^{+0}$	6.32×10^{-2}
324.5	4.7	$3.70 \times 10^{+0}$	4.17×10^{-2}
333.9	4.7	$3.14 \times 10^{+0}$	3.85×10^{-2}
343.3	4.7	$2.46 \times 10^{+0}$	2.71×10^{-2}
352.7	4.7	$1.79 \times 10^{+0}$	2.32×10^{-2}
362.1	4.7	$1.18 \times 10^{+0}$	1.33×10^{-2}
371.5	4.7	7.95×10^{-1}	1.08×10^{-2}
380.9	4.7	4.73×10^{-1}	8.32×10^{-2}
390.3	4.7	2.79×10^{-1}	6.38×10^{-3}
399.7	4.7	1.34×10^{-1}	4.38×10^{-3}
409.1	4.7	6.12×10^{-2}	2.93×10^{-3}
418.5	4.7	2.84×10^{-2}	2.03×10^{-3}
427.9	4.7	1.28×10^{-2}	1.38×10^{-3}
437.4	4.7	3.48×10^{-3}	7.47×10^{-3}
446.8	4.7	1.49×10^{-3}	8.65×10^{-4}
456.2	4.7	5.80×10^{-4}	3.36×10^{-4}

Table 4

The transverse-energy differential cross-section $d\sigma/dE_T$ in the full region for 200 GeV per nucleon ^{32}S-Pt collisions

E_T [GeV]	Bin half-width [GeV]	$d\sigma/dE_T$ [mb/GeV]	Error [mb/GeV]
32.9	14.1	$1.39 \times 10^{+1}$	$7.63 \times 10^{+0}$
61.1	14.1	$8.23 \times 10^{+0}$	$1.77 \times 10^{+0}$
89.4	14.1	$9.31 \times 10^{+0}$	$1.54 \times 10^{+0}$
117.6	14.1	$9.29 \times 10^{+0}$	$1.35 \times 10^{+0}$
145.8	14.1	$6.30 \times 10^{+0}$	$1.10 \times 10^{+0}$
174.0	14.1	$6.40 \times 10^{+0}$	$1.03 \times 10^{+0}$
202.2	14.1	$6.81 \times 10^{+0}$	$1.05 \times 10^{+0}$
221.0	4.7	$5.93 \times 10^{+0}$	$3.38 \times 10^{+1}$
230.4	4.7	$5.93 \times 10^{+0}$	3.38×10^{-1}
239.8	4.7	$5.30 \times 10^{+0}$	3.19×10^{-1}
249.2	4.7	$4.53 \times 10^{+0}$	2.95×10^{-1}
258.6	4.7	$5.43 \times 10^{+0}$	3.23×10^{-1}
268.1	4.7	$5.51 \times 10^{+0}$	3.26×10^{-1}
277.5	4.7	$4.86 \times 10^{+0}$	3.06×10^{-1}
286.9	4.7	$5.27 \times 10^{+0}$	3.19×10^{-1}
296.3	4.7	$5.25 \times 10^{+0}$	3.18×10^{-1}
305.7	4.7	$4.66 \times 10^{+0}$	3.00×10^{-1}
315.1	4.7	$5.26 \times 10^{+0}$	3.19×10^{-1}
324.5	4.7	$4.71 \times 10^{+0}$	3.02×10^{-1}
333.9	4.7	$3.72 \times 10^{+0}$	2.68×10^{-1}
343.3	4.7	$3.61 \times 10^{+0}$	2.64×10^{-1}
352.7	4.7	$2.85 \times 10^{+0}$	1.05×10^{-1}
362.1	4.7	$2.07 \times 10^{+0}$	8.89×10^{-2}
371.5	4.7	$1.34 \times 10^{+0}$	7.12×10^{-2}
380.9	4.7	8.63×10^{-1}	5.68×10^{-2}
390.3	4.7	4.56×10^{-1}	4.10×10^{-2}
399.7	4.7	2.35×10^{-1}	2.91×10^{-2}
409.1	4.7	1.56×10^{-1}	2.34×10^{-2}
418.5	4.7	4.83×10^{-2}	1.29×10^{-2}
427.9	4.7	1.42×10^{-2}	3.46×10^{-3}
437.4	4.7	8.12×10^{-3}	2.57×10^{-3}
446.8	4.7	3.14×10^{-3}	1.57×10^{-3}

Table 5

The transverse-energy differential cross-section $d\sigma/dE_T$ in the full region for 200 GeV per nucleon ^{32}S–Pb collisions

E_T [GeV]	Bin half-width [GeV]	$d\sigma/dE_T$ [mb/GeV]	Error [mb/GeV]
44.2	4.9	$1.73 \times 10^{+1}$	$1.83 \times 10^{+0}$
54.1	4.9	$1.22 \times 10^{+1}$	$1.43 \times 10^{+0}$
73.7	14.7	$9.41 \times 10^{+0}$	$7.35 \times 10^{+0}$
103.2	14.7	$8.53 \times 10^{+0}$	5.98×10^{-1}
132.7	14.7	$6.94 \times 10^{+0}$	5.17×10^{-1}
162.2	14.7	$7.06 \times 10^{+0}$	4.77×10^{-1}
191.7	14.7	$5.79 \times 10^{+0}$	4.21×10^{-1}
211.4	4.9	$6.40 \times 10^{+0}$	7.64×10^{-1}
221.2	4.9	$6.29 \times 10^{+0}$	7.93×10^{-1}
231.0	4.9	$5.40 \times 10^{+0}$	7.11×10^{-1}
240.9	4.9	$5.79 \times 10^{+0}$	2.49×10^{-1}
250.7	4.9	$5.73 \times 10^{+0}$	2.48×10^{-1}
260.5	4.9	$5.38 \times 10^{+0}$	2.40×10^{-1}
270.4	4.9	$5.23 \times 10^{+0}$	2.37×10^{-1}
280.2	4.9	$5.57 \times 10^{+0}$	2.47×10^{-1}
290.0	4.9	$5.60 \times 10^{+0}$	2.46×10^{-1}
299.9	4.9	$4.95 \times 10^{+0}$	2.31×10^{-1}
309.7	4.9	$5.59 \times 10^{+0}$	2.45×10^{-1}
319.5	4.9	$5.37 \times 10^{+0}$	2.41×10^{-1}
329.4	4.9	$4.61 \times 10^{+0}$	2.23×10^{-1}
339.2	4.9	$4.35 \times 10^{+0}$	2.17×10^{-1}
349.0	4.9	$3.60 \times 10^{+0}$	1.97×10^{-1}
358.9	4.9	$2.79 \times 10^{+0}$	1.73×10^{-1}
368.7	4.9	$1.79 \times 10^{+0}$	1.38×10^{-1}
378.5	4.9	$1.29 \times 10^{+0}$	1.21×10^{-1}
388.4	4.9	8.01×10^{-1}	4.02×10^{-1}
398.2	4.9	3.34×10^{-1}	2.41×10^{-2}
408.0	4.9	1.34×10^{-1}	1.56×10^{-2}
417.9	4.9	5.20×10^{-2}	9.05×10^{-2}
427.7	4.9	2.30×10^{-2}	6.31×10^{-3}
442.4	9.8	9.30×10^{-3}	9.30×10^{-3}

Table 6

The transverse-energy differential cross-section $d\sigma/dE_T$ in the full region for 200 GeV per nucleon ^{32}S–U collisions

E_T [GeV]	Bin half-width [GeV]	$d\sigma/dE_T$ [mb/GeV]	Error [mb/GeV]
37.6	9.4	$9.72 \times 10^{+0}$	$4.93 \times 10^{+0}$
51.7	4.7	$1.20 \times 10^{+1}$	$6.39 \times 10^{+0}$
61.1	4.7	$6.80 \times 10^{+0}$	$6.67 \times 10^{+0}$
70.5	4.7	$9.36 \times 10^{+0}$	$4.91 \times 10^{+0}$
79.9	4.7	$4.62 \times 10^{+0}$	$3.96 \times 10^{+0}$
98.8	14.1	$5.64 \times 10^{+0}$	$2.46 \times 10^{+0}$
117.6	4.7	$6.20 \times 10^{+0}$	$3.07 \times 10^{+0}$
136.4	14.1	$4.12 \times 10^{+0}$	$2.95 \times 10^{+0}$
155.2	4.7	$3.82 \times 10^{+0}$	$2.29 \times 10^{+0}$
164.6	4.7	$9.24 \times 10^{+0}$	$2.86 \times 10^{+0}$
174.0	4.7	$5.65 \times 10^{+0}$	$2.34 \times 10^{+0}$
183.4	4.7	$5.95 \times 10^{+0}$	$2.25 \times 10^{+0}$
192.8	4.7	$6.83 \times 10^{+0}$	$2.33 \times 10^{+0}$
202.2	4.7	$3.36 \times 10^{+0}$	$1.64 \times 10^{+0}$
211.6	4.7	$5.68 \times 10^{+0}$	$2.05 \times 10^{+0}$
221.0	4.7	$6.84 \times 10^{+0}$	$4.45 \times 10^{+0}$
230.4	4.7	$5.49 \times 10^{+0}$	4.16×10^{-1}
239.8	4.7	$5.77 \times 10^{+0}$	4.14×10^{-1}
249.2	4.7	$5.65 \times 10^{+0}$	4.05×10^{-1}
258.6	4.7	$4.99 \times 10^{+0}$	3.85×10^{-1}
268.1	4.7	$5.92 \times 10^{+0}$	4.19×10^{-1}
277.5	4.7	$5.17 \times 10^{+0}$	3.92×10^{-1}

(Cont.)

Table 6 (Cont.)

E_T [GeV]	Bin half-width [GeV]	$d\sigma/dE_T$ [mb/GeV]	Error [mb/GeV]
286.9	4.7	$5.55 \times 10^{+0}$	4.06×10^{-1}
296.3	4.7	$5.52 \times 10^{+0}$	4.00×10^{-1}
305.7	4.7	$5.79 \times 10^{+0}$	4.10×10^{-1}
315.1	4.7	$5.88 \times 10^{+0}$	4.14×10^{-1}
324.5	4.7	$5.47 \times 10^{+0}$	3.99×10^{-1}
333.9	4.7	$4.43 \times 10^{+0}$	3.59×10^{-1}
343.3	4.7	$4.92 \times 10^{+0}$	3.78×10^{-1}
352.7	4.7	$4.04 \times 10^{+0}$	1.53×10^{-1}
362.1	4.7	$3.57 \times 10^{+0}$	1.44×10^{-1}
371.5	4.7	$2.62 \times 10^{+0}$	1.23×10^{-1}
380.9	4.7	$2.11 \times 10^{+0}$	1.10×10^{-1}
390.3	4.7	$1.60 \times 10^{+0}$	9.60×10^{-1}
399.7	4.7	$1.18 \times 10^{+0}$	8.23×10^{-2}
409.1	4.7	6.82×10^{-1}	6.22×10^{-2}
418.5	4.7	4.43×10^{-1}	2.50×10^{-2}
427.9	4.7	2.61×10^{-1}	1.91×10^{-2}
437.4	4.7	1.73×10^{-1}	1.55×10^{-2}
446.8	4.7	8.90×10^{-2}	1.10×10^{-2}
456.2	4.7	4.33×10^{-2}	7.65×10^{-2}
465.6	4.7	2.13×10^{-2}	5.34×10^{-3}
475.0	4.7	6.58×10^{-3}	2.94×10^{-3}
484.4	4.7	2.59×10^{-3}	1.83×10^{-3}

Table 7

The transverse-energy differential cross-section $d\sigma/dE_T$ in the full region for 200 GeV per nucleon ^{16}O–W collisions

E_T [GeV]	Bin half-width [GeV]	$d\sigma/dE_T$ [mb/GeV]	Error [mb/GeV]
124.6	2.4	$6.92 \times 10^{+0}$	$2.31 \times 10^{+0}$
129.3	2.4	$1.05 \times 10^{+1}$	$1.00 \times 10^{+0}$
134.0	2.4	$9.71 \times 10^{+0}$	9.67×10^{-1}
138.7	2.4	$9.34 \times 10^{+0}$	9.48×10^{-1}
143.4	2.4	$1.04 \times 10^{+1}$	$1.00 \times 10^{+0}$
148.1	2.4	$8.58 \times 10^{+0}$	9.10×10^{-1}
152.8	2.4	$8.97 \times 10^{+0}$	9.31×10^{-1}
157.5	2.4	$7.05 \times 10^{+0}$	8.25×10^{-1}
162.2	2.4	$7.82 \times 10^{+0}$	8.69×10^{-1}
166.9	2.4	$6.47 \times 10^{+0}$	7.91×10^{-1}
171.6	2.4	$7.05 \times 10^{+0}$	8.25×10^{-1}
176.4	2.4	$5.79 \times 10^{+0}$	7.48×10^{-1}
181.1	2.4	$6.56 \times 10^{+0}$	7.95×10^{-1}
185.8	2.4	$4.91 \times 10^{+0}$	6.88×10^{-1}
190.5	2.4	$5.96 \times 10^{+0}$	7.57×10^{-1}
195.2	2.4	$4.60 \times 10^{+0}$	6.64×10^{-1}
199.9	2.4	$4.40 \times 10^{+0}$	6.48×10^{-1}
204.6	2.4	$2.29 \times 10^{+0}$	4.67×10^{-1}
209.3	2.4	$2.09 \times 10^{+0}$	4.45×10^{-1}
214.0	2.4	$1.89 \times 10^{+0}$	4.22×10^{-1}
218.7	2.4	$1.07 \times 10^{+0}$	1.42×10^{-1}
223.4	2.4	8.96×10^{-1}	1.29×10^{-1}
228.1	2.4	6.86×10^{-1}	1.13×10^{-1}
232.8	2.4	3.68×10^{-1}	8.23×10^{-2}
237.5	2.4	2.92×10^{-1}	7.30×10^{-2}
242.2	2.4	1.27×10^{-1}	4.78×10^{-2}
246.9	2.4	7.16×10^{-2}	3.58×10^{-2}
251.6	2.4	3.55×10^{-2}	2.51×10^{-2}
256.3	2.4	3.51×10^{-2}	2.48×10^{-2}
265.7	2.4	1.03×10^{-2}	5.93×10^{-3}
270.4	2.4	3.38×10^{-3}	3.38×10^{-3}

Table 8

The maximum stopping fractions (S_{max}) for ^{16}O–W (at 200 GeV per nucleon) and for collisions of ^{32}S on Al, Ag, W, Pt, Pb, and U (at 200 GeV per nucleon) in $-0.1 < \eta_{lab} < 5.5$

	O–W	S–Al	S–Ag	S–W	S–Pt	S–Pb	S–U
E_T [GeV]	264	192	353	445	435	432	472
E_T^{avail} [GeV]	300	343	420	502	504	506	530
S_{max}	0.88	0.56	0.84	0.88	0.87	0.86	0.89

Figure captions

Fig. 1: The energy of the neighbouring strips compared with the central strip ULAC as a function of strip number: a) for incident ^{32}S at 200 GeV per nucleon, b) for incident 200 GeV protons. For a strip, the energy is summed for the three hadronic sections.

Fig. 2: Transverse-energy differential cross-section, $d\sigma/dE_T$, in the full region for 200 GeV per nucleon ^{32}S on Al, Ag, W, Pt, Pb, and U collisions.

Fig. 3: The differential cross-section $d\sigma/dE_T$ for ^{32}S–W collisions at 200 GeV per nucleon in the full (▲), forward (▼), and backward (full squares) regions. The predictions for FRITIOF (continuous line) and IRIS (dashed line) are shown for the backward and full regions. Also shown is the IRIS prediction (dashed line) for the forward region. The horizontal error bars indicate the systematic error of 7% on the E_T scale.

Fig. 4: Contour plot of the differential cross-section $d^2\sigma/(dE_T^{back}E_T^{forw})$ for the production of E_T in the backward region, and of E_T in the forward region at 200 GeV per nucleon. Successive contours are separated by a factor 1/e. The IRIS prediction for one contour is shown as a dashed line.

Fig. 5: Comparison between the E_T distributions over the full region for ^{16}O–W (full squares) and ^{32}S–W (▲) at 200 GeV per nucleon.

Fig. 6: Distribution of E_T as a function of pseudorapidity, normalized to the number of events, for three values of E_T in the full region (plateau, shoulder, and tail) at 200 GeV per nucleon for a) ^{16}O–W and b) ^{32}S–W collisions. IRIS predictions (dashed lines) are shown for E_T values at the same $d\sigma/dE_T$ as the corresponding data.

Fig. 7: The first and second moments of the pseudorapidity distributions as well as $(dE_T/d\eta)_{max}$ versus E_T in the full region for ^{16}O–W and ^{32}S–W collisions. The solid line indicates the FRITIOF prediction.

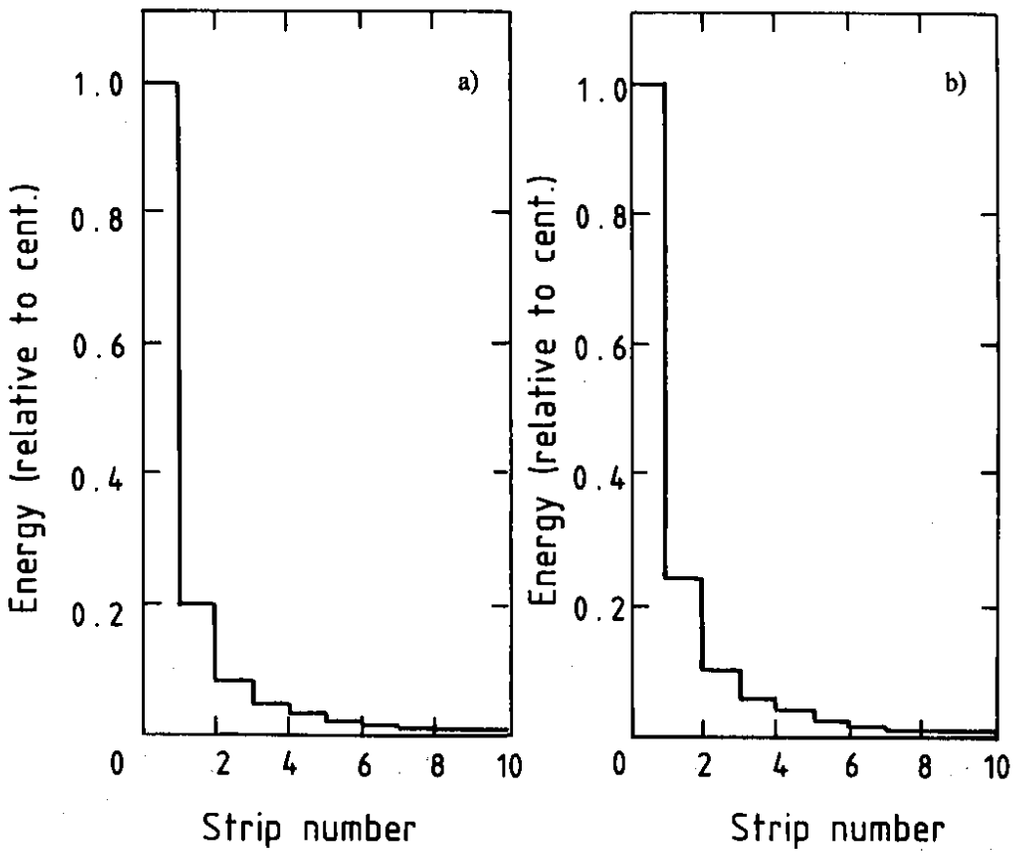
a)
b)
Energy (relative to cent.)
Energy (relative to cent.)
1.0
0.8
0.6
0.4
0.2
0
2
4
6
8
10
Strip number
Strip number

Fig. 1

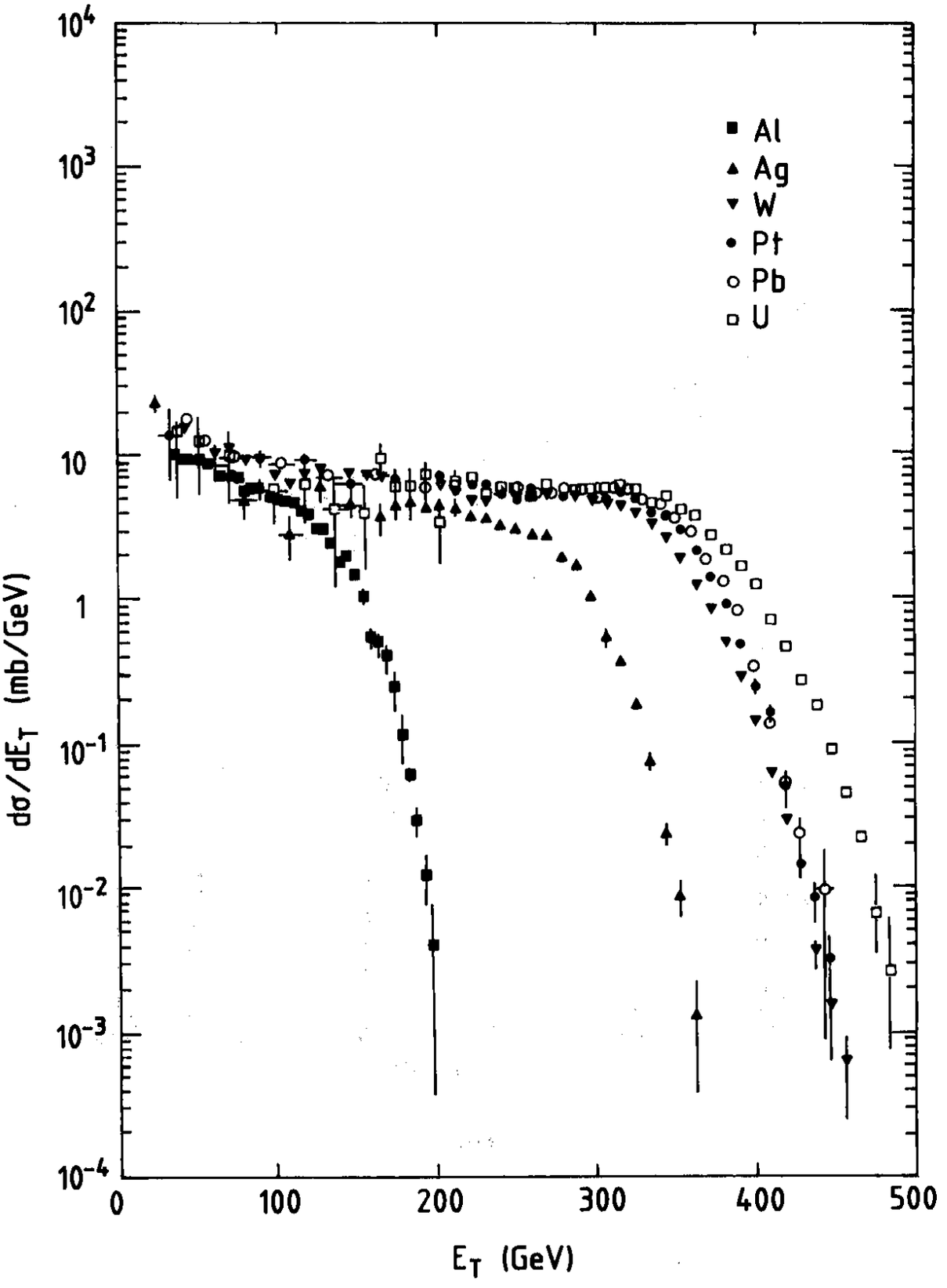
Al
Ag
W
Pt
Pb
U
$d\sigma/dE_T$ (mb/GeV)
E_T (GeV)
10^4
10^3
10^2
10
1
10^{-1}
10^{-2}
10^{-3}
10^{-4}
0
100
200
300
400
500

Fig. 2

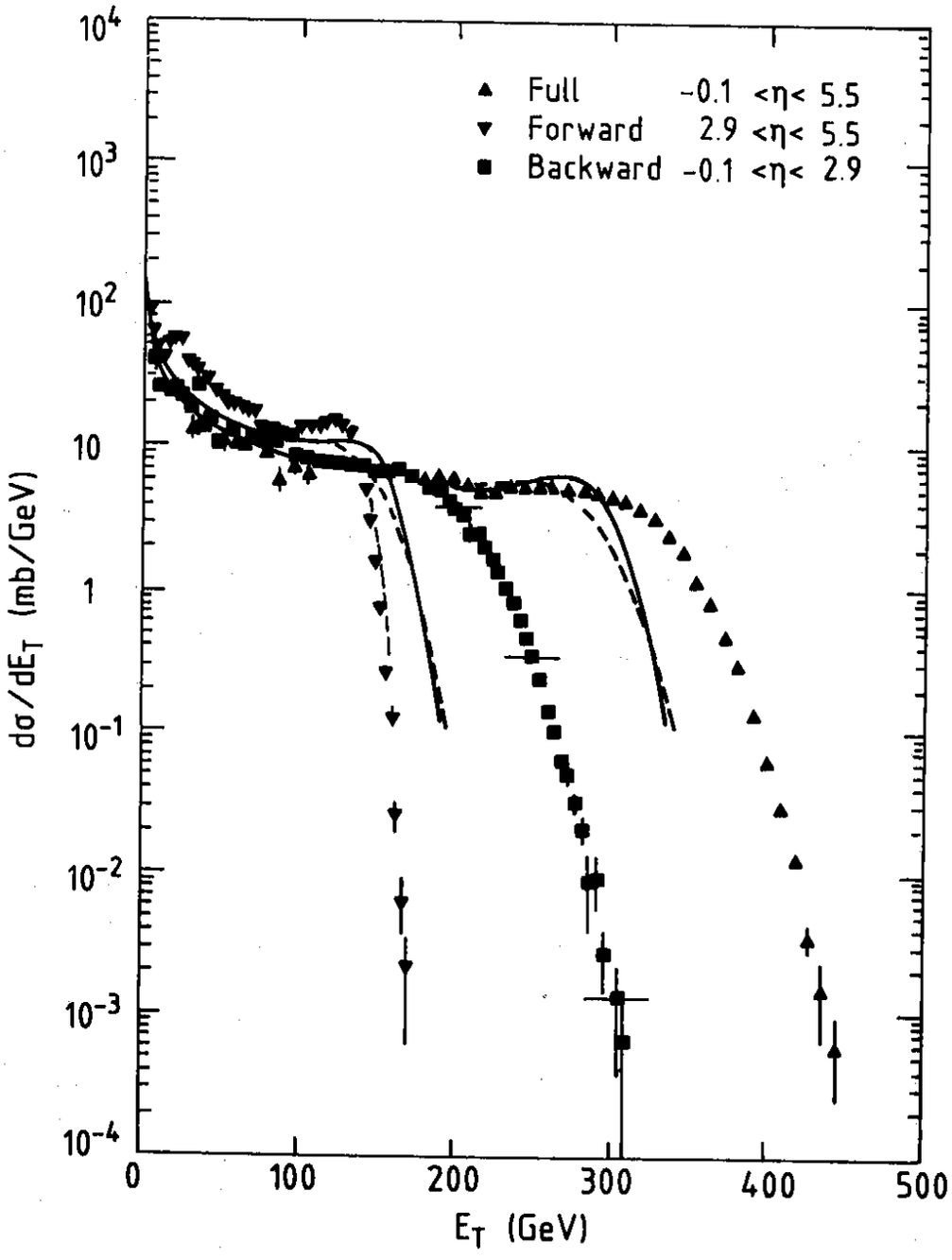
Full -0.1 <η< 5.5
Forward 2.9 <η< 5.5
Backward -0.1 <η< 2.9
dσ/dE_T (mb/GeV)
E_T (GeV)
10^4
10^3
10^2
10
1
10^-1
10^-2
10^-3
10^-4
0
100
200
300
400
500

Fig. 3

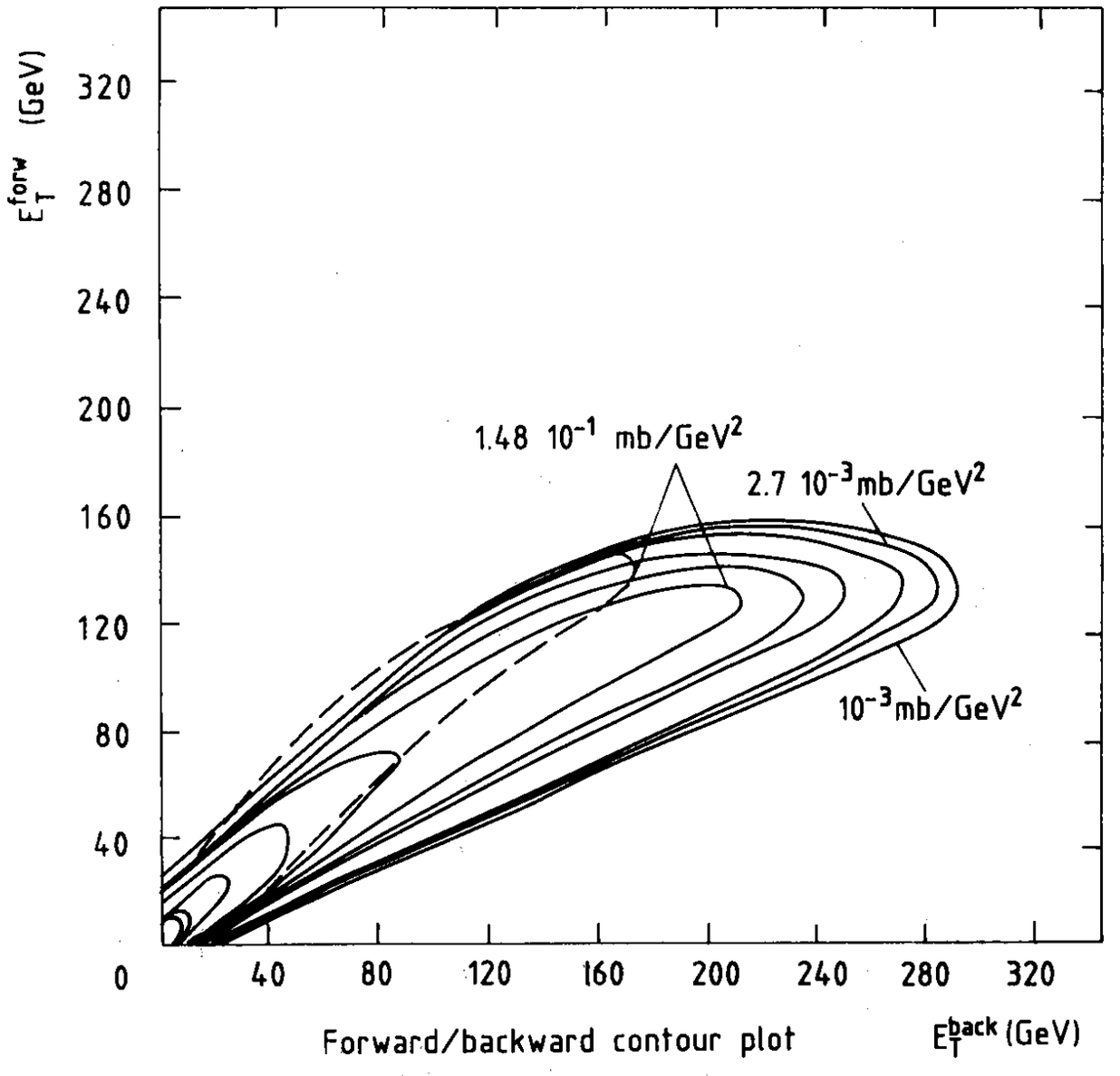
E_T^{forw} (GeV)
320
280
240
200
160
120
80
40
0
40
80
120
160
200
240
280
320
1.48 10^{-1} mb/GeV^2
2.7 10^{-3}mb/GeV^2
10^{-3}mb/GeV^2
Forward/backward contour plot
E_T^{back} (GeV)

Fig. 4

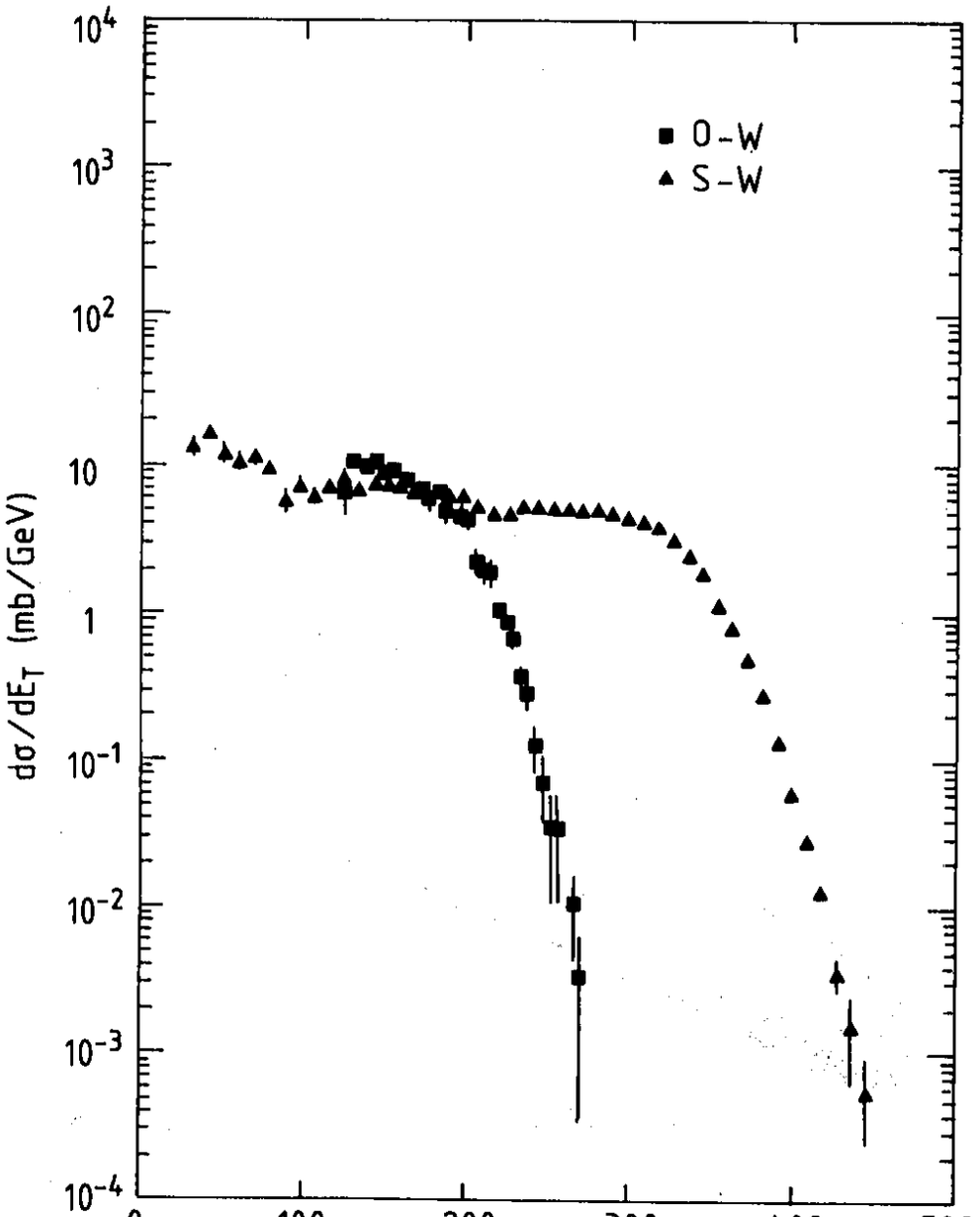
O-W
S-W
10^4
10^3
10^2
10
1
10^{-1}
10^{-2}
10^{-3}
10^{-4}
$d\sigma/dE_T$ (mb/GeV)
0
100
200
300
400
500
E_T (GeV)

Fig. 5

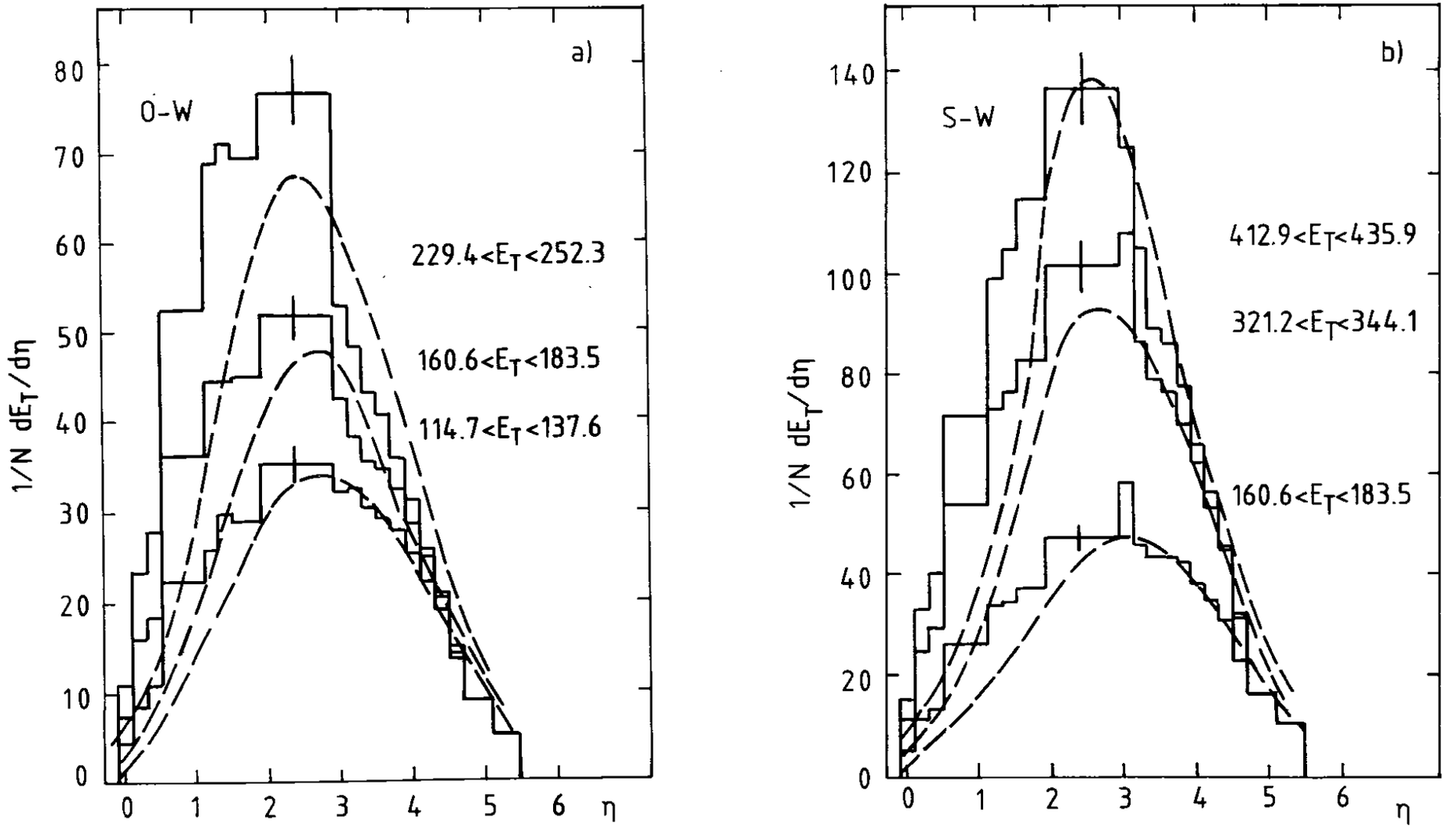
a)
O-W
229.4<E_T<252.3
160.6<E_T<183.5
114.7<E_T<137.6
1/N dE_T/dη
η
b)
S-W
412.9<E_T<435.9
321.2<E_T<344.1
160.6<E_T<183.5
1/N dE_T/dη
η

Fig. 6

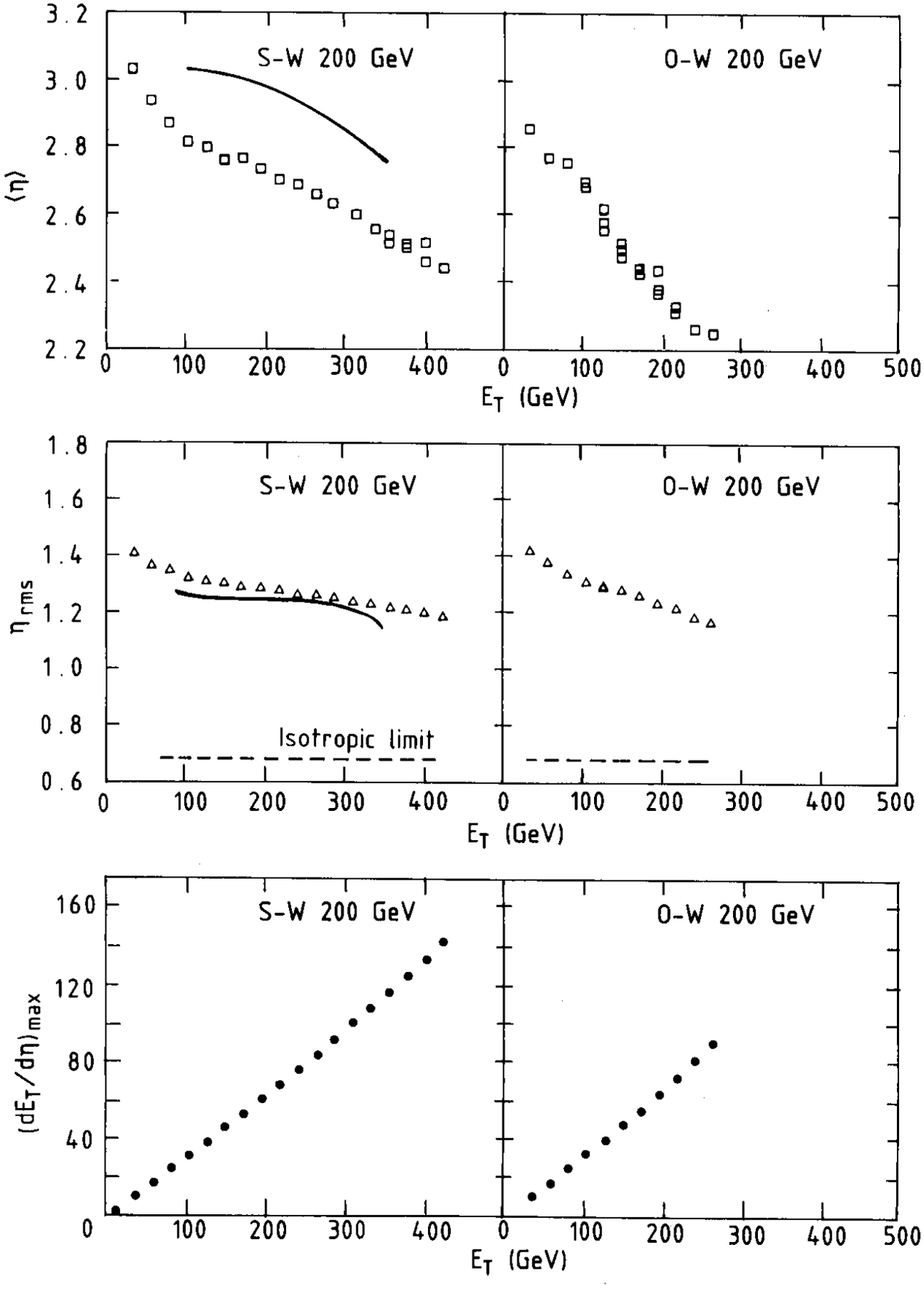

Fig. 7

Imprimé au CERN. Prix : 0.80 Fr.